CrossMark

JM PAPERS

The Rayleigh prolongation factor at small bubble to wall stand-off distances

Fabian Reuter[1],†,‡**, Qingyun Zeng**[2],†,‡ **and Claus-Dieter Ohl**[1]

[1]Department Soft Matter, Faculty of Natural Sciences, Institute for Physics, Otto-von-Guericke University Magdeburg, 39106 Magdeburg, Germany

[2]School of Mechanical and Aerospace Engineering, Nanyang Technological University, 50 Nanyang Avenue, Singapore 639798, Republic of Singapore

The Rayleigh collapse time is the time it would take to shrink an empty spherical bubble in an infinite liquid domain to zero size, which is a function of ambient pressure and initial bubble radius. If a solid boundary is located in the vicinity of the shrinking or collapsing bubble, then liquid flow is hindered, such that the collapse time is prolonged. This can be quantified with the Rayleigh prolongation factor k. Here, we provide k for intermediate to smallest bubble to wall stand-off distances. It is measured with single laser-induced cavitation bubbles in water close to a solid boundary. Maximum bubble radii are determined from microscopic high-speed imaging at one million frames per second. Collapse times are measured acoustically via the acoustic transients emitted during bubble seeding and collapse. The experimental findings are compared, with good agreement, to numerical simulations based on a volume of fluid method. As a result, a polynomial fit of k versus stand-off distance is given for the near-wall bubble collapse in water. Then the influence of the viscosity on k is studied numerically in the near-wall regime.

Key words: cavitation, bubble dynamics

1. Introduction

A starting point for modern research in cavitation dates back to 1917 when Rayleigh provided a theoretical description for the collapse of a spherical void in an unbounded domain of incompressible and non-viscous liquid (Rayleigh 1917). The resulting model can be considered the most basic description of cavitation bubble dynamics. Recently, analytical (Kudryashov & Sinelshchikov 2014) and approximate analytical (Obreschkow,

† Email addresses for correspondence: fabian.reuter@ovgu.de, qzeng001@e.ntu.edu.sg
‡ Both authors contributed equally to the manuscript.

Bruderer & Farhat 2012) solutions for the model have been reported, and the equation of bubble oscillation has even been solved for more than three dimensions (Klotz 2013). Rayleigh's derivation uses the conservation of energy, where the potential energy of the fully expanded and empty bubble at ambient pressure p_a is converted to kinetic energy within a spherical converging flow field. Given that the bubble is initiated with radius R_{max}, the Rayleigh collapse time T_C – i.e. the time until the bubble reaches radius zero – can be derived from the continuity equation and the integration of the energy equation:

$$T_C^{Rayleigh} = 0.91468\,R_{max}\sqrt{\rho/p_a}, \tag{1.1}$$

where ρ denotes the mass density of the liquid. The proportionality constant 0.91468 is called the Rayleigh factor. Experiments with single cavitation bubbles *per se* do not start with a void at maximum radius R_{max}; instead, these bubbles are seeded from a small radius by depositing energy into a small liquid volume that induces a rapid bubble growth, e.g. through a liquid–vapour phase transition. The energy may be deposited by an underwater detonation, a spark discharge or a focused laser pulse ('optic cavitation'). The latter technique offers excellent precision on the location of bubble nucleation, and with suitable measures, also excellent repeatability. As a result, at maximum expansion, an almost empty and spherical bubble is formed, sharing its centre with the location of the initial energy deposition. Then the pressure difference between bubble interior and the ambient pressure drives and accelerates the shrinkage of the bubble. This phase of the flow is commonly termed the bubble collapse. The temporal radius evolution and time to collapse are very well predicted by the Rayleigh model and the Rayleigh collapse time $T_C^{Rayleigh}$ (Lauterborn 1972). Under the assumption of Rayleigh collapse, where the liquid is inviscid and the collapsing flow is spherical, the expansion and the collapse phases are symmetrical. Thus we can define the bubble lifetime from the nucleation to collapse as $T_L^{Rayleigh} = 2T_C^{Rayleigh}$.

In most technical applications with cavitation, however, the bubbles are collapsing at and interacting with material boundaries. There exists an unlimited variety of boundaries. They can be of any geometry and mechanical compliance. From the unlimited variety of boundaries, we chose a planar and rigid wall with dimensions much larger than the bubble dimensions. Such a boundary restricts the liquid flow around the collapsing bubble, and as a consequence, the collapsing bubble develops a rich and non-spherical dynamics together with a complex flow field. A prominent feature is the radial jet that pierces the bubble, shapes it toroidally, and impacts onto the boundary (Plesset & Chapman 1971; Lauterborn & Bolle 1975; Lauterborn & Kurz 2010). Ring vortices can be formed and can spread along the boundary (Brujan *et al.* 2002; Reuter *et al.* 2017). And with a bubble close to a solid body, significant wall-normal forces and large wall shear stresses can be induced onto the boundary (Krasovitski & Kimmel 2004; Dijkink & Ohl 2008; Vos *et al.* 2011; Reuter & Mettin 2018; Zeng *et al.* 2018a). These forces may be exploited or avoided, depending on the use case, e.g. they may be beneficial in ultrasonic cleaning, laser ablation of liquids, or cavitation peening, but are unwanted in cavitation erosion. The precise bubble dynamics is known to depend sensitively on the stand-off distance d of the bubble to the boundary, which is commonly non-dimensionalized by the maximum radius of the bubble as $\gamma = d/R_{max}$ (a sketch is given in figure 1). The significant regime for cavitation material interaction can be considered to be in the range $\gamma < 4$, where the long-ranging vortex ring still reaches the boundary (Reuter, Cairós & Mettin 2016), but for smaller stand-offs, the interaction with the boundary tends to be more intense. Recently, for closest distances to a solid boundary ($\gamma < \approx 0.2$), a needle jet with
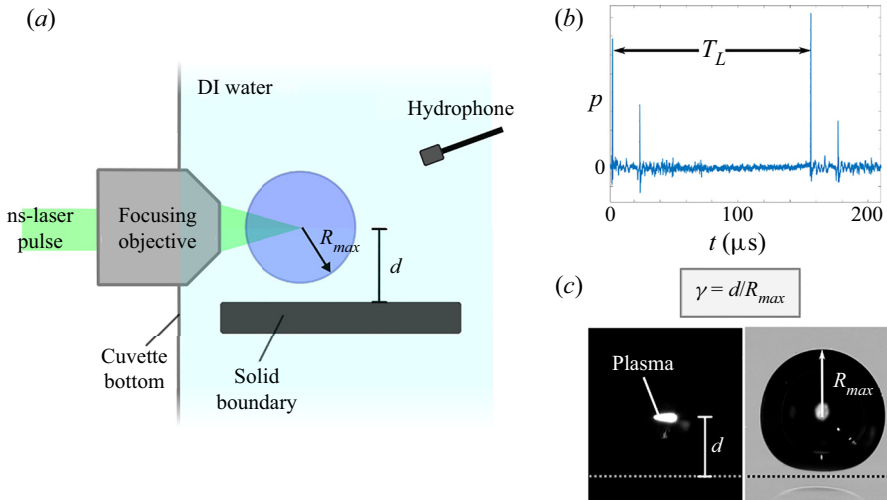
Figure 1. (*a*) Experimental set-up. The bubble is high-speed imaged from the same perspective as sketched here, in the direction perpendicular to the plane of the paper. (*b*) Example of the hydrophone signal used for the measurement of T_L. (*c*) Definition and measurement of γ. The images show the plasma spark during seeding (left) and the instance of maximum bubble expansion (right), with the rigid boundary located horizontally at the bottom.

an impact velocity of over 900 m s^{-1} was predicted numerically (Lechner *et al.* 2019) and found experimentally (Reuter & Ohl 2021). This particular small-distance regime is exploited for the production of nanoparticles by laser ablation in liquids in combination with cavitation bubbles (Barcikowski *et al.* 2019). While this small stand-off regime is likely the most relevant for many applications, the Rayleigh lifetime is valid only for large distances, i.e. $\gamma \to \infty$. To derive the lifetime for a bubble at an infinitely extended rigid boundary with potential flow, Rattray (1951) accounted for the bubble deformation and centroid motion, and obtained with perturbation theory for $\gamma \gg 1$ a modified Rayleigh collapse time $T_C = k \, T_C^{Rayleigh}$ with prolongation factor $k(\gamma) = 1 + 0.205/\gamma$ (Plesset & Chapman 1971). Shima & Tomita (1981) report on the work of Sato & Shima (1980), who included surface tension and found, by employing a variational method, a similar factor $k = 1 + 0.190/\gamma$ for water. These factors k, however, are valid only for $\gamma \gg 1$ and weak bubble deformations. In potential flow, for $\gamma \to \infty$ the prolongation factor must approach unity, for decreasing γ the prolongation factor must first increase, and for $\gamma \to 0$ the prolongation factor should approach unity again, as the flow field of the hemispherical collapse is of spherical symmetry again. Thus there must be a local maximum of k as a function of γ.

A few experimental studies reported on the prolongation factor at intermediate stand-offs (Fujikawa & Akamatsu 1978; Shima & Tomita 1981; Godwin *et al.* 1999; Shaw, Schiffers & Emmony 2001; Chen *et al.* 2011), with only few of them including smaller stand-offs ($\gamma \lesssim 0.6$) (Vogel, Lauterborn & Timm 1989; Gregorčič, Petkovšek & Možina 2007). So far only Yang, Wang & Keat (2013) report experimental measurements of the Rayleigh prolongation factor from a larger number of of data points based on single laser-induced bubbles in water. Thus for probably the most relevant regime of cavitation material interaction, there are currently very few experimental data available, which do not allow us to deduce a quantitative description of k.

The collapse time should be affected further by the viscosity of the liquid, already in the spherical case but in addition via viscosity-dependent bubble shapes in the near-wall regime (Hupfeld *et al.* 2020; Zeng, An & Ohl 2022).

Here, we measure the prolongation factor for single laser-induced bubbles of millimetre size in water for $\gamma \to 0$, and compare it with direct numerical simulations using a volume of fluid method. With validated numerics, we study computationally the influence of the viscosity on k.

2. Methods

The experimental set-up is shown in figure 1(*a*). A single bubble is produced in deionized (DI) water with a nanosecond-long laser pulse (Litron nano S, frequency-doubled Nd:YAG) in a glass cuvette (dimensions approximately $50 \times 50 \times 80$ mm^3; the open surface in the sketch is located vertically on the right). At the focus, a plasma is generated and a spherical bubble develops. Focusing through the cuvette bottom is achieved with a submerged long-working-distance microscope (Mitutoyo 50x, $NA = 0.42$, nominal working distance 20.5 mm, in-house modified with water-tight sealing) after beam expansion. The bubble is generated close to a polished metal slab (2 mm thick brass or stainless steel, 25×25 mm^2) that serves as the rigid boundary. To vary the stand-off distance to the boundary, the metal slab is attached to a motor-controlled micrometre stage. Focusing the laser parallel to the solid boundary avoids the formation of spurious bubbles from the residual light that was not absorbed within the plasma at the laser focus.

A needle PVDF hydrophone (Müller-Platte Needle Probe, rise time ≈ 50 ns) is positioned at a distance of about 4.5 mm from the spot of plasma generation. The hydrophone is connected to an oscilloscope (Teledyne LeCroy WavePro 404HD) operating at sampling frequency 1 GHz, with internal low pass with cut-off frequency 500 MHz. In the acoustic measurements, the instances of bubble generation and bubble collapse become detectable easily as distinct peaks from their respective shock wave emission. The delay between the peaks allows the measurement of T_L; an example is shown in figure 1(*b*). This approach is possible as the propagation velocity of the shock waves from seeding and collapse are the same. This is confirmed by tracking the respective shock fronts in a high-speed imaging series with a large field of view of several millimetres (not shown). The reason is that the shock wave propagation velocity approaches the speed of sound already after a few hundred micrometres (Vogel, Busch & Parlitz 1996), which is less than 10 % of the distance to the hydrophone, and both shock waves are of similar peak pressures. The two main peaks in the image are each followed by a smaller one after about $t_d = 21$ μs from the reflection of the shock wave at the cuvette boundaries, the water surface and in particular the focusing objective. This was also confirmed by schlieren high-speed imaging of the shock front (not shown here). Using the speed of sound in water, the time delay $t_d = 21$ μs corresponds to a travelled distance of 3.15 cm, indicating a distance 1.58 cm to the nearest cuvette boundary. The bubble shape dynamics is recorded with a long-working-distance microscope objective or a macro lens (Mitutoyo 5x long working distance microscope objective or Canon MP-E 65 mm) with a high-speed camera (Shimadzu HPV-X2) operating at one million frames per second. The exposure time is effectively set as short as 220 fs as the scene is illuminated with a short laser pulse (Ekspla Femtolux, wavelength 515 nm) delivered via a glass fibre. The timing is controlled via a pulse generator (BNC 525, Berkeley Nucleonics, CA) using a LabView script developed to measure the selected stand-off range automatically. The data are evaluated
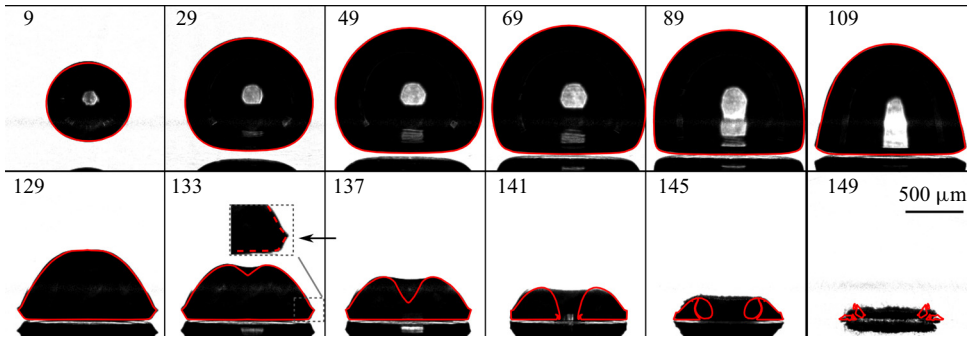
Figure 2. Comparison of experimental and numerical bubble dynamics for the case $\gamma = 0.64$. The numerical bubble interface in red is overlaid on the experimental image. Times indicated are in µs. The lifetime of the bubble T_L is 150.76 µs in the experimental and 150.42 µs in the numerical case. The maximum radii are $R_{max} = 681$ µm in the experiment and 685 µm in the simulation, respectively. The rigid boundary is oriented horizontally in the bottom of the frame, and shows a mirror image of the bubble in the experimental case. The arrow indicates the kink in the bubble.

with Matlab and ImageJ. In total, 142 bubbles covering a stand-off range $0.02 < \gamma < 1.03$ were evaluated with mean maximum radius 749 µm and standard deviation 40 µm. The position of bubble generation is highly repeatable to better than one pixel or 3.56 µm or 5.50 µm, respectively, depending on the imaging objective. We estimate the error in pixel resolution to 1 %. To exclude any potential influence from cavitation erosion on the metal slab, after each bubble event, the slab is moved to a pristine position.

To compare the experimental result, we simulate the laser-induced bubble as a gas bubble using a compressible volume of fluids (VoF) solver accounting for both viscosity and surface tension. The expansion and shrinkage of the bubble during the first cycle can be described with a polytropic equation of state with specific heat ratio $\kappa = 1.4$. Although the bubble content is different from the experiment, where the cavitation bubble is a mixture of vapour and various gases (Lauterborn & Kurz 2010), this treatment has been well validated in our previous works on bubble collapse near a single wall (Zeng *et al.* 2018*a*) and within a thin gap (Zeng, Gonzalez-Avila & Ohl 2020), as well from other groups (Popinet & Zaleski 2002; Koch *et al.* 2016; Li *et al.* 2019). The numerical bubble starts from a spherical gas pocket with radius 50 µm and high pressure. This pressure is determined based on the comparison in figure 2, where both the size and period of growth and collapse of the bubble are about the same as the experimental result. The initial pressure is found to be 1400 bar and is kept the same for the following studies. When the bubble reaches maximum expansion, it starts to collapse from the pressure difference $\Delta p = p_a - p_i$, where p_a is the ambient pressure, and p_i is the pressure of the bubble interior. We insert Δp for p_a in (1.1), which then reads $T_C^{Rayleigh} = 0.91468\, R_{max}\sqrt{\rho/(p_a - p_i)}$. In the simulations at maximum expansion, p_i fluctuates between 2448 Pa and 2744 Pa for all simulations carried out here. This is close to the interior pressure expected in the experimental case, which is the water vapour pressure $p_v = 2339$ Pa. In the following, we use $p_v \approx p_i$, and calculate the Rayleigh lifetime in all cases according to

$$T_C^{Rayleigh} = 0.91468\, R_{max}\sqrt{\rho/(p_a - p_v)}. \tag{2.1}$$

Thirty bubbles in the stand-off range $\gamma = 0.05$ to $\gamma = 1.5$ were simulated with mean maximum radius 699 µm and standard deviation 34 µm. For details on the simulations, we

refer the reader to Zeng *et al.* (2018*b*, 2020). The numerical bubble lifetime is measured from $t = 0$, i.e. the beginning of the simulation to the collapse, which is considered as the instance of minimum gas phase volume that coincides with the shock wave emission as well as the numerical seeding. Experimental and numerical definitions of T_L then can be considered the same if the seeding volumes are equal in both cases. Numerically, the bubble is initialized with radius 50 μm, which is chosen based on the size of the plasma in the experiment.

The maximum discrepancy between the definitions is negligible as estimated in the following way. A lower boundary for the bubble wall velocity $\dot{R}(t)$ at seeding is given by the simulations as 250 m s^{-1}, yielding a difference of less than 100 ns between the numerical and experimental measurements, which corresponds to less than 0.125 % of T_L. Thus experimental and numerical procedures on the measurement of the lifetime yield the same results within the experimental uncertainties. The measurements of R_{max} and stand-off distance are depicted in figure 1(*c*). Even though widely used, the definition of the stand-off γ raises some ambiguities when non-spherical bubbles close to boundaries are studied. In the experiments, we define the bubble centre as the centre of the plasma region; see figure 1(*c*). Also, R_{max} is taken as the distance between the bubble centre and the point reached by the bubble interface farthest from the boundary over the full high-speed framing sequence (which turns out to be identical to the instance of maximum bubble volume). The distance to the boundary d is measured from the centre of the plasma region to the boundary. To determine the boundary position, an appropriate image of the time series is chosen once the bubble and the reflected image of the bubble are visible simultaneously. The boundary location is the location of the mirror axis. This yields a well-defined and robust measurement of γ. In the theoretical derivations of Rayleigh, due to the energy ansatz, the bubble volume plays a special role, and often an alternative definition of γ is used, where R_{max}^{Veq} is taken as an equivalent radius of a sphere that has the same volume as the deformed bubble at maximum (volumetric) expansion.

We benchmark both definitions with our numerical results in Appendix A by calculating the difference between the volumetric definition γ^V and the geometric definition γ used for the experimental data: $\Delta\gamma = \gamma^V - \gamma$. It turns out that $0.009 < \Delta\gamma < 0.023$ in the stand-off interval 0.05 to 1.50. Thus for our purposes, both definitions can be considered to yield almost identical results. In the present experiment, the uncertainty in the measurement of γ is smaller than 0.023, when assuming an uncertainty of 0.5 pixels for measurements of each of the boundary position, the plasma position and the location of the bubble wall, and using the pixel resolution 3.56 μm px^{-1}.

3. Results and discussion

We start with a validation of the numerical simulation by comparing the time evolution of the bubble shapes; see figure 2. The computed bubble interfaces are drawn as red contours superimposed on the experimental images at the same time instance. Times are given in μs. Then the bubble is generated at $t = 0$, and collapses at T_L. The experiment and simulation have very close T_L values, which are 150.76 μs and 150.42 μs, respectively. The interframe time of the first six frames is constant at 20 μs; from $t = 120$ μs onwards, the interframe time is reduced to resolve the fast collapse dynamics. Note that during the expansion, the bubble acquires a hemispherical shape with its low interface flattened. Then during the collapse, the axial jet indents and pierces the bubble from the

944 A11-6

boundary-distant pole. At $t = 145\ \mu s$, the bubble interface appears rugged, which is a result of splashing within the bubble following the jet impact onto the boundary. Please note that the numerical image provides a cut through the bubble shape, which allows us to see the jet indentation in the central axis, while in the experimental image, the toroidal shape is projected in the viewing direction. Thus for the first bubble oscillation, experimental and numerical bubble shapes are in excellent agreement. This is the case for the entire stand-off range under investigation here.

From these data, experimentally and numerically, using the acoustic measurement of shock wave emission, the prolongation factor $k = T_L/T_L^{Rayleigh}$ of the lifetime of non-spherical bubbles as compared to the Rayleigh collapse time is measured. Here, $T_L^{Rayleigh}$ is calculated using (2.1), using mass density $\rho = 998\ \text{kg m}^{-3}$ and ambient pressure $p_a = 101.325$ kPa. The measured Rayleigh prolongation factor k is presented in figure 3 as a function of the stand-off distance. Regarding the trend, experimental and numerical data show excellent agreement over the entire considered stand-off range. However, the numerics predict a k that is about 2.5 % larger than the experimental findings. As the main reason that contributes to an overestimation of the numerical collapse time, we identify the shock waves that are emitted during bubble seeding. These are reflected at the domain boundaries and are focused back, much stronger than in the experiment due to the cylindrical symmetry. This reduces mainly R_{max} but not T_L to the same extent, thus increasing k. In the experimental data, k may be underestimated as the rigid plane is not extended infinitely but is provided by a metal slab of finite dimensions where the bubble has at least a distance 4 mm to the closest edge here. An additional systematic error may stem from an error in the imaging scale that we estimate at 1 %, which would effect k linearly. A 7th-degree polynomial $k^{fit} = \sum_{i=0}^{7} p_i \gamma^i$ is fitted to the experimental data:

$$k^{fit}(\gamma) = 0.9777 + 1.427\gamma - 4.504\gamma^2 + 8.562\gamma^3 - 9.66\gamma^4 + 6.102\gamma^5$$
$$- 1.991\gamma^6 - 0.2619\gamma^7. \tag{3.1}$$

This fit is valid in the γ range $0 < \gamma < 1.0$. Here, the root-mean-square error of the fit is 0.0068. As anticipated, the lifetime increases as the bubble is brought closer to the boundary from infinity. A maximum increase in lifetime is observed for $\gamma = 0.69$; thereafter, T_L decreases monotonically. Indeed, at $\gamma = 0$, the prolongation factor approaches approximately 1, and the fit yields $k^{fit}(\gamma = 0) = 0.978$. For comparison, Rattray's corrections up to first (Rattray 1951; Plesset & Chapman 1971) and second (Rattray 1951) order, as well as the correction of Sato & Shima (1980), are plotted. They are valid only for weak bubble deformations, which explains the divergence from the measured curve in particular for $\gamma < 1$. The overestimation for $\gamma > 1$ is due mainly to the different definitions of R_{max} and R_{max}^{Veq}. In Appendix A, this effect is discussed further, and for comparison, k is presented normalized on the volumetric equivalence radius R_{max}^{Veq}. There, we also compare our data with the volumetric numerical data given by Lechner *et al.* (2020). The reduction of the collapse time in the range $\gamma < 0.69$ is caused by the approach of the bubble dynamics towards the hemispherical case. The Rayleigh collapse time implies a spherical flow field, which results in the fastest way to collapse a spherical bubble and thus yields the shortest lifetime. The same holds by symmetry considerations for the hemispherical collapse $\gamma = 0$ when viscosity is neglected. Thus, in particular, the hemispherical case is characterized by boundary parallel flows, which in the case of a
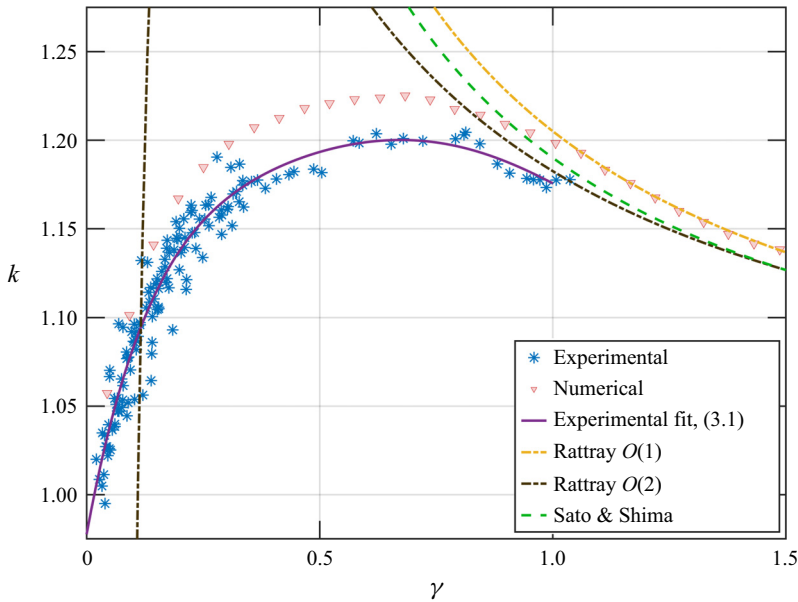
Figure 3. Rayleigh prolongation factor obtained experimentally and numerically. The purple line is a numerical fit to both data with a polynomial of 7th degree. The dashed lines show the Rattray corrections of first and second order, $k_R^{O(1)}(\gamma) = 1 + 0.205/\gamma$ and $k_R^{O(2)}(\gamma) = 1 + 0.205/\gamma - 0.0225/\gamma^2$, as well as the Sato & Shima correction for water, $k_S(\gamma) = 1 + 0.19/\gamma$.

viscous liquid, such as water, can be identified via kinks in the bubble wall (see the arrow in figure 2, at $t = 133$ μs). The smaller γ, the earlier the kink appears during the dynamics, because the bubble centre reaches the boundary earlier. Consistently with the maximum of k around $\gamma = 0.69$ found here, the kinks were shown to appear only for $\gamma < 0.73$, for the bubbles under consideration (Reuter & Ohl 2021). The flows associated with the kinks can become so dominant for smallest γ that they converge and collide at the axis of symmetry even before the regular jet from the apex passes the respective point on the axis. Then a supersonic needle jet is formed in the direction towards the boundary (Lechner *et al.* 2019, 2020; Reuter & Ohl 2021).

For a comparison of our data with the data available in the literature, see figure 4; an overview of R_{max} is given in table 1. All studies employed laser-induced single bubbles in water and measured the bubble lifetime by acoustic means via detection of the shock wave with different techniques. It should be noted, though, that it seems no work so far had focused in particular on a precise measurement of the Rayleigh prolongation factor in the very small stand-off distance regime. Accordingly, the measurement data available show some significant scatters, and it is difficult to derive a clear trend. Some data sets are based on measurements on differently sized bubbles. In addition, many authors do not specify how the normalized stand-off distance was measured, and sometimes inexact maximum radii where given. For the data provided in Yang *et al.* (2013), we have calculated average values for k to reduce scatter and number of data points. For comparison, our fit is plotted as a solid line. The fit lies in between the literature data, which can be taken as a confirmation of the data, but in addition for $\gamma < 0.6$ shows a clear trend to $k \rightarrow 1$.
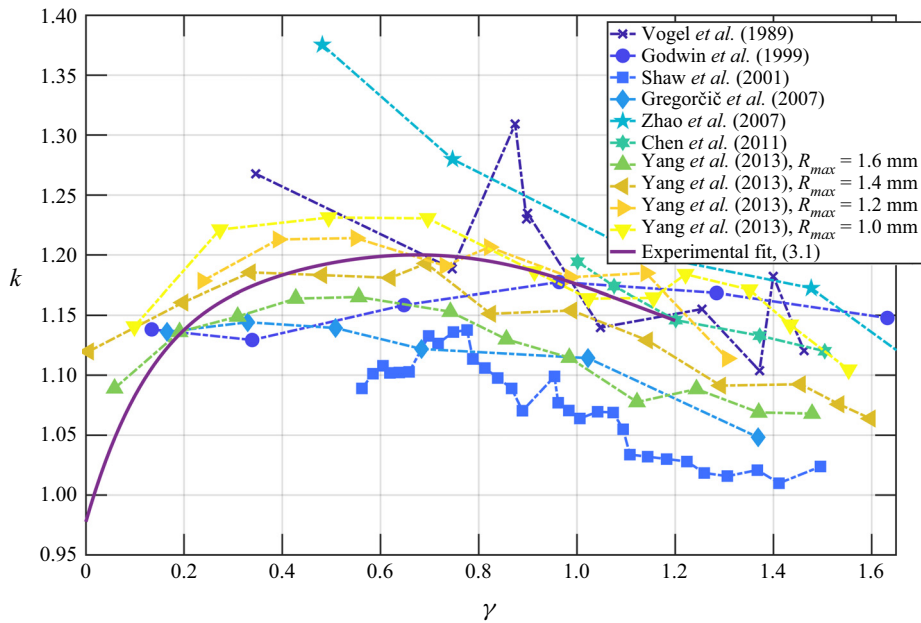
944 A11-8

Figure 4. Comparison of Rayleigh prolongation factors obtained experimentally by several authors on single laser-induced bubbles in water.

Reference	R_{max} (mm)	Remarks
Vogel *et al.* (1989)	1.6–4.5	
Godwin *et al.* (1999)	Not specified	
Shaw *et al.* (2001)	1.09–1.85	γ was tuned by changing the bubble size via the laser energy (at two fixed stand-off distances); T_L was rounded to 10 µm.
Gregorčič *et al.* (2007)	< 1.6	For $\gamma \rightarrow \infty$, $R_{max} = 1.55$ mm; for all other cases, $R_{max} <$ 1.60 mm. Distance to free surface is 10 times R_{max}.
Zhao *et al.* (2007)	Not specified	$R_{max} = 2.6$ mm in one case.
Chen *et al.* (2011)	2.00–3.00	Authors report that they controlled the bubble size from 2.00 mm and 3.00 mm to achieve $\gamma = 1.0–1.5$.
Yang *et al.* (2013)	1.0–1.6	Four maximum radii, as indicated.

Table 1. Overview of experimental parameters in the studies reported in figure 4.

4. Influence of liquid viscosity and maximum radius

Besides the shown stand-off dependence of k, the bubble lifetime may also depend on the viscosity of liquid μ and to some extend on R_{max} through viscous forces (Ivany & Hammitt 1965; Brennen 2014). We now fix $R_{max} \approx 700$ µm according to our experimental values, and vary the viscosity. One example of the dynamics is shown in figure 5, where we compare the bubble shapes in liquids with two selected viscosities $\mu = 10^{-3}$ Pa s and $\mu = 0.02$ Pa s for the same stand-off distance $\gamma = 0.52$. In general, the two bubbles undergo similar deformation, but in the liquid with $\mu = 0.02$ Pa s, the bubble expands and collapses more slowly as the drag force owing to viscosity increases. In both cases, during expansion the bubbles acquire a similar hemispherical shape, yet some details of
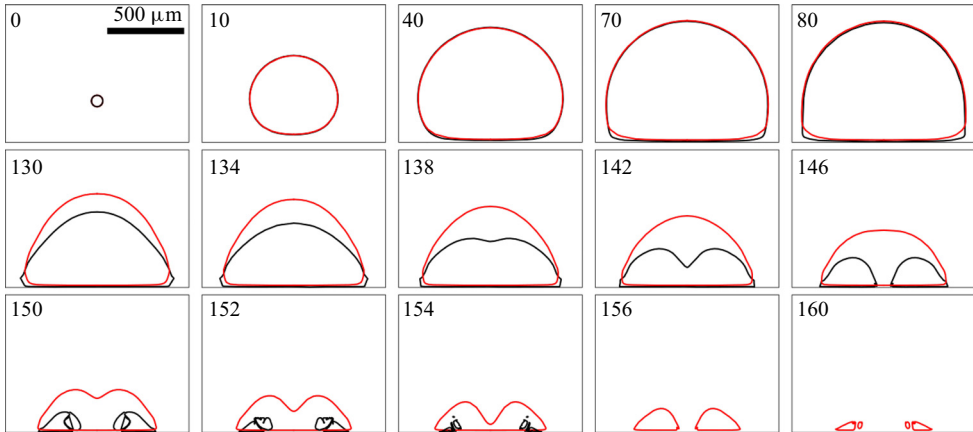
Figure 5. Comparison of numerical bubble shape dynamics for two viscosities, $\mu_1 = 1$ mPa s (black contours) and $\mu_2 = 20$ mPa s (red contours), with $\gamma = 0.52$.

bubble deformation are modified by the higher viscosity. For example, the thickness h of the liquid layer between wall and bubble has increased from about 4 µm to 20 µm, as a thicker boundary layer has developed (Schlichting & Gersten 2003).

We now present the prolongation factor $k(\gamma)$ for six viscosities, $\mu = 10^{-3}$, 0.01, 0.02, 0.03, 0.04 and 0.06 Pa s, in figure 6. Viscosity in general and viscous boundary layers are expected to retard the collapse and thus to increase the prolongation factor k for all γ values. This occurs monotonically. Still, for all viscosities, k drops quickly for $\gamma \lesssim 0.25$, i.e. when the bubble approaches the hemispherical collapse. At intermediate distances from the boundary, $0.25 < \gamma < \gamma_m$, k grows slowly to the peak value at γ_m where the collapse time is longest. For increasing viscosities, this maximum is seen for larger stand-offs, as with higher viscosities the influence of the boundary ranges further into the liquid. For $\gamma > \gamma_m$, the lower bubble wall is further from the boundary and thus affected less by the viscous boundary layer. This results in a decrease of k with γ. Eventually, for $\gamma \to \infty$, k is expected to approach a minimum that is a function of R_{max} and μ (Proussevitch & Sahagian 1998).

Next, we explore the dependency on R_{max} and fix the viscosity at $\mu = 1$ mPa s. In figure 7, k is shown for three maximum radii. All three curves show qualitatively the same behaviour but are scaled by some factor.

In an effort to estimate the respective scalings, we consider a spherical bubble and the normal viscous stresses $p_\mu = 4\pi\mu\dot{R}/R$ (Franc 2007) at the bubble interface. Then (2.1) reads

$$T_C^\mu = 0.91468\, R_{max}\sqrt{\rho/(\Delta p - p_\mu)}, \tag{4.1}$$

where $\Delta p = p_a - p_v$. With characteristic radius $R = R_{max}$ and deformation rate $\dot{R} = R_{max}/T_C^{Rayleigh}$, one obtains a viscosity modified collapse time T_C^μ, and consequently a viscosity modified prolongation factor for the spherical case:

$$k^{\gamma \to \infty}(\mu, R_{max}) = \frac{T_C^\mu}{T_C^{Rayleigh}} = \left(\sqrt{1 - \frac{4\pi}{0.915\sqrt{\rho\,\Delta p}}\frac{\mu}{R_{max}}}\right)^{(-1/2)} \approx 1 + \frac{2\pi}{0.915\sqrt{\rho\,\Delta p}}\frac{\mu}{R_{max}}, \tag{4.2}$$

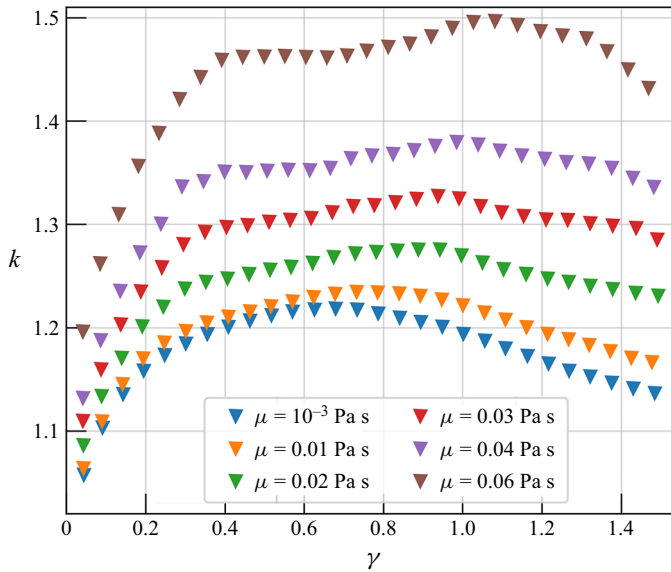where for the approximation, the square root has been linearized.

944 A11-10

Figure 6. Comparison of the factor k as a function of γ for bubbles in liquid of six different viscosities ($R_{max} = 700\ \mu\text{m}$).
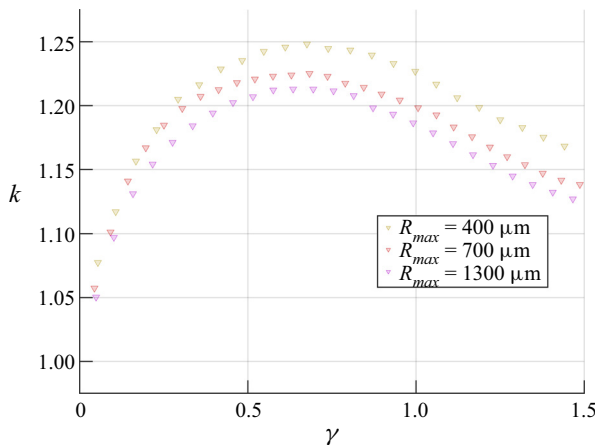

Figure 7. Numerical measurements of the prolongation factor k as function of the stand-off distance γ for three different maximum radii R_{max}.

However, this scaling clearly fails to predict the results, in particular as it largely underestimates the prolongation factor. For example in figure 7, (4.2) would predict a negligible factor of only 1.0012 between $k(R_{max} = 1300\ \mu\text{m})$ and $k(R_{max} = 400\ \mu\text{m})$, while the numerical results show a factor of around 1.036 between the two curves. To understand if the prolonged collapse time is due to viscous dissipation in the boundary layer, we conducted simulations where the boundary condition at the wall has been altered to free slip. Interestingly, even at the higher viscosities, this had only a minor influence on k for $\gamma < 0.9$, and did not affect significantly the prolongation factor at all for $\gamma > 0.9$. Thus the prolongation due to viscosity stems from the entire non-spherical flow field, which is

944 A11-11

known to have a complex structure (Zeng *et al.* 2022). This observation may help to derive an appropriate scaling of the prolongation factor that accounts for viscosity, too.

5. Conclusions

We measured experimentally and numerically the prolongation factor k of the lifetime of a single cavitation bubble that collapses near a rigid boundary in water. Simulations and experiment show the trend of $k(\gamma)$ in excellent agreement, but the simulation predicts a value about 2.5 % larger for all stand-offs. The longest lifetime in water is found for $\gamma = 0.69$ in both the numerics and experiments with $k \approx 1.2$. It decreases quickly for smaller stand-off distances where the dynamics approaches an ideal hemispherical collapse. The numerical parameter study of $k(\gamma)$ for smaller ratios R_{max}/μ shows, besides a general increase of the prolongation factor, a shift of the maximum collapse time towards larger stand-offs. Even though during most of the bubble lifetime – i.e. up to a few microseconds before the bubble collapse – similar bubble shapes are observed independently of the viscosity, a general scaling over a wide range of maximum radii and viscosities seems difficult, as the substantial viscous dissipation is associated with the entirety of the complex, non-spherical flow field. These experimentally confirmed data could be useful for the validation of numerical simulations of single bubble dynamics, for evaluation of the distance of bubbles for surface treatment and particle generation (Soyama 2015; Barcikowski *et al.* 2019), and to test advanced analytical models of the collapse at small stand-off distances.

Declaration of interests. The authors report no conflict of interest.

Author ORCIDs.

Ⓓ Fabian Reuter https://orcid.org/0000-0002-8908-4209;

Ⓓ Qingyun Zeng https://orcid.org/0000-0003-1369-8236;

Ⓓ Claus-Dieter Ohl https://orcid.org/0000-0001-5333-4723.

Appendix A. On the definition of γ and the prolongation factor for the equivalent volumetric maximum radius R_{max}^{Veq}

In figure 8, the Rayleigh case of a bubble at a boundary is shown. The geometric definition of R_{max} as we use it throughout this paper and explain in the experimental section is appropriate to describe the hemispherical collapse (figure 8a). For comparison, the definition of the maximum radius from a volume equivalent is shown too; see figure 8(b). In that case, the bubble is described by a sphere of an effectively smaller radius. The two radii are related by $R_{max}^{Veq} = \sqrt[3]{\frac{1}{2}} R_{max}$ for this ideal Rayleigh case of bubbles of spherical cap shape.

In figure 9, we show the same data as in figure 3, but this time as functions of γ^V and scaled on R_{max}^{Veq}, i.e. $k_{Veq} = T_L/(0.1837\,R_{max}^{Veq}\mathrm{m}^{-1}\,\mathrm{s})$. As expected, in the range $\gamma > 1$, the measured data fit the theoretical predictions by Rattray or Sato & Shima better as the latter are based on a volumetric definition. For $\gamma \to 0$, the deviations from the theoretical descriptions again are large, and k_{Veq} does not approach a prolongation factor of unity for
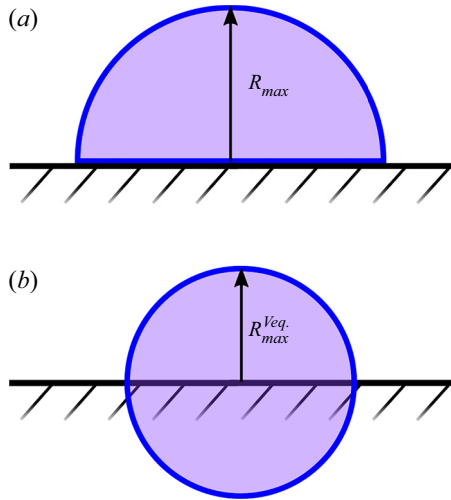
Figure 8. Definition of the maximum bubble radius for the Rayleigh case at $\gamma = 0$. The hemispherical bubble with radius R_{max} in (*a*), in the volume equivalent description in (*b*) is considered as an entire sphere of smaller radius R_{max}^{Veq}.
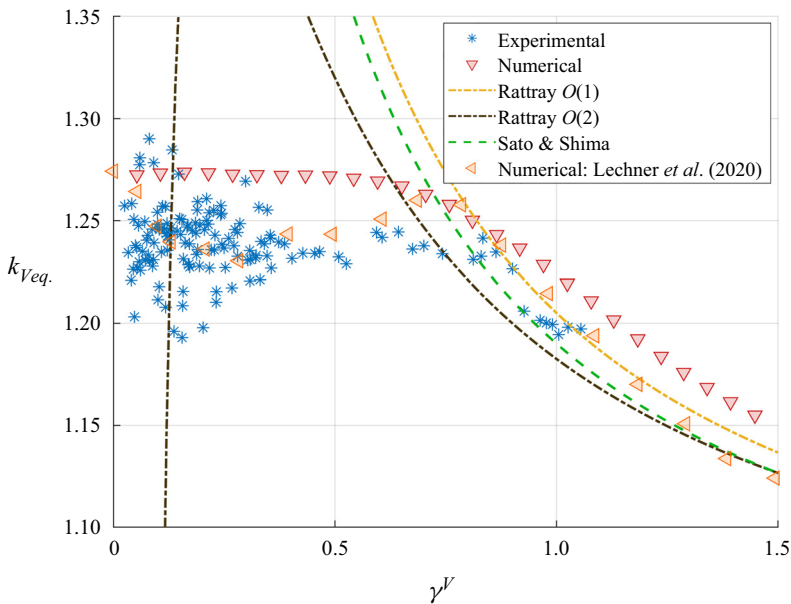

Figure 9. Rayleigh prolongation factor obtained experimentally and numerically as in figure 3 but now normalized on the equivalent volumetric maximum bubble radius R_{max}^{Veq}. The dashed lines show the Rattray corrections of first and second order, $k_R^{O(1)}(\gamma) = 1 + 0.205/\gamma$ and $k_R^{O(2)}(\gamma) = 1 + 0.205/\gamma - 0.0225/\gamma^2$, as well as the Sato & Shima correction for water, $k_S(\gamma) = 1 + 0.19/\gamma$. The red triangles show numerical results from Lechner *et al.* (2020).

the hemispherical case but seems to approach $\sqrt[3]{2}$. This is because effectively, it predicts the collapse time of a bubble of the smaller radius R_{max}^{Veq}.
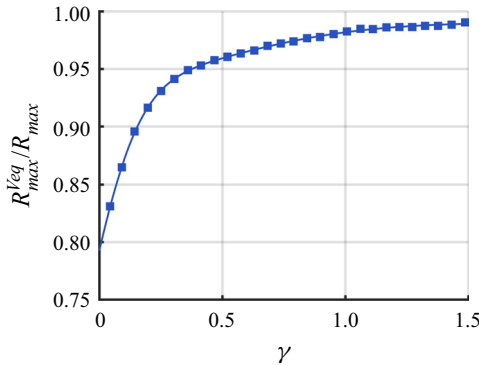
Figure 10. Numerical results relating the volume equivalent radius R_{max}^{Veq} to the geometric maximum radius R_{max}, and the fit with parameters given in (A1), as a function of γ.

While k has a maximum at $\gamma = 0.69$, with this scaling, k_{Veq} rather shows a plateau when $\gamma \to 0$. This is because with decreasing γ, the value of R_{max}^{Veq} decreases as the bubble volume decreases, as sketched in figure 8.

In figure 9 the numerical results by Lechner *et al.* (2020) are plotted additionally (orange triangles). They agree well in trend and in values with our results. However, an additional fluctuation with a local minimum around $\gamma = 0.25$ is seen, which is not present in our data. Kindly note that their data was normalized on a fixed value of $R_{max} = 500\,\mu\text{m}$ measured on one free bubble, neglecting the effects of the boundary on the bubble size. Furthermore, their data is measured on the collapse phase only and not over the entire bubble life time; for details see Lechner *et al.* (2020).

In the following, we work out the relationship between the volumetric and geometric definitions, and also give a conversion function derived from our simulations that we used to re-scale our experimental data in figure 9. This is justified by the perfect matching of bubble shapes at maximum expansion (see figure 2). In figure 10, the relation R_{max}^{Veq}/R_{max} is shown together with the fit function given in (A1) below. For the fit, we use a rational of the form $p_1 x^4 + p_2 x^3 + p_3 x^2 + p_4 x + p_5)/(x^4 + q_1 x^3 + q_2 x^2 + q_3 x + q_4)$, and find the fit parameters

$$R_{max}^{Veq}/R_{max} = \frac{0.9526\gamma^4 + 0.1514\gamma^3 + 0.4080\gamma^2 + 0.09755\gamma + 0.06398}{\gamma^4 + 0.006959\gamma^3 + 0.5873\gamma^2 + 0.02949\gamma + 0.08072}, \quad (A1)$$

with a root-mean-square error 0.0008 in the range shown in figure 10. For $\gamma = 0$, the fit yields, as expected, $0.06398/0.08072 = 0.793 \approx 0.7937 = \sqrt[3]{\frac{1}{2}}$. The data also allow us to convert γ to γ^V easily according to $\gamma^V = \gamma R_{max}/R_{max}^{Veq}$; the numerical results are shown in figure 11. Finally, we consider the difference in stand-off values between the volumetric and geometric stand-off definitions, $\gamma^V - \gamma$; see figure 12. It turns out that the difference between the definitions is below 0.022 for all stand-offs. This small value is often negligible and within the range of measurement errors. The maximum radius, however, varies for both definitions up to a factor $\approx 2^{1/3}$ (at $\gamma = 0$).

Note that for $\gamma \to \infty$, both definitions are the same. Here we chose to use the geometric definition because it allows the correct prediction of the collapse time for $\gamma = 0$ and $\gamma \to \infty$, and we feel that it is the adequate description for the hemisphere, while with
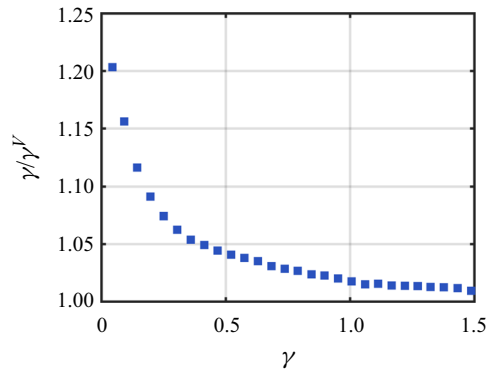
944 A11-14

Figure 11. Numerical conversion factor between geometric and volumetric normalization of the stand-off as a function of γ.
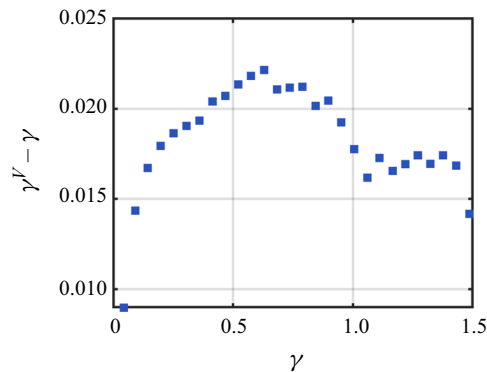

Figure 12. Difference between the geometric and volumetric stand-offs γ and γ^V. The difference is smaller than 0.023 in all cases, which is negligible most of the time.

the volumetric stand-off, this is only the case for $\gamma \to \infty$. In addition, the geometric definition offers some experimental advantages that we use here because it is sufficient to measure the bubble boundary at only one position, while for a volumetric measurement the boundary needs to be determined along the entire bubble contour, along which, typically, the illumination conditions change, in particular when close to the solid.

REFERENCES

BARCIKOWSKI, S., PLECH, A., SUSLICK, K.S. & VOGEL, A. 2019 Materials synthesis in a bubble. *MRS Bull.* **44** (5), 382–391.

BRENNEN, C.E. 2014 *Cavitation and Bubble Dynamics*. Cambridge University Press.

BRUJAN, E.A., KEEN, G.S., VOGEL, A. & BLAKE, J.R. 2002 The final stage of the collapse of a cavitation bubble close to a rigid boundary. *Phys. Fluids* **14** (1), 85–92.

CHEN, J., HAN, B., LI, B.-B., SHEN, Z.-H., LU, J. & NI, X.-W. 2011 The collapse of a bubble against infinite and finite rigid boundaries for underwater laser propulsion. *J. Appl. Phys.* **109** (8), 083101.

DIJKINK, R. & OHL, C.-D. 2008 Measurement of cavitation induced wall shear stress. *Appl. Phys. Lett.* **93** (25), 254107.

FRANC, J.-P. 2007 The Rayleigh–Plesset equation: a simple and powerful tool to understand various aspects of cavitation. In *Fluid Dynamics of Cavitation and Cavitating Turbopumps*, pp. 1–41. Springer.

FUJIKAWA, S. & AKAMATSU, T. 1978 Experimental investigations of cavitation bubble collapse by a water shock tube. *Bull. JSME* **21** (152), 223–230.

GODWIN, R.P., CHAPYAK, E.J., NOACK, J. & VOGEL, A. 1999 Aspherical bubble dynamics and oscillation times. In *Laser–Tissue Interaction X: Photochemical, Photothermal, and Photomechanical*, vol. 3601, pp. 225–236. International Society for Optics and Photonics.

GREGORČIČ, P., PETKOVŠEK, R. & MOŽINA, J. 2007 Investigation of a cavitation bubble between a rigid boundary and a free surface. *J. Appl. Phys.* **102** (9), 094904.

HUPFELD, T., LAURENS, G., MERABIA, S., BARCIKOWSKI, S., GÖKCE, B. & AMANS, D. 2020 Dynamics of laser-induced cavitation bubbles at a solid–liquid interface in high viscosity and high capillary number regimes. *J. Appl. Phys.* **127** (4), 044306.

IVANY, R.D. & HAMMITT, F.G. 1965 Cavitation bubble collapse in viscous, compressible liquids – numerical analysis. *J. Basic Engng* **87** (4), 977–985.

KLOTZ, A.R. 2013 Bubble dynamics in *n* dimensions. *Phys. Fluids* **25** (8), 082109.

KOCH, M., LECHNER, C., REUTER, F., KÖHLER, K., METTIN, R. & LAUTERBORN, W. 2016 Numerical modeling of laser generated cavitation bubbles with the finite volume and volume of fluid method, using openfoam. *Comput. Fluids* **126**, 71–90.

KRASOVITSKI, B. & KIMMEL, E. 2004 Shear stress induced by a gas bubble pulsating in an ultrasonic field near a wall. *IEEE Trans. Ultrason. Ferroelectr. Freq. Control* **51** (8), 973–979.

KUDRYASHOV, N.A. & SINELSHCHIKOV, D.I. 2014 Analytical solutions of the Rayleigh equation for empty and gas-filled bubble. *J. Phys.* A*: Math. Theor.* **47** (40), 405202.

LAUTERBORN, W. 1972 High-speed photography of laser-induced breakdown in liquids. *Appl. Phys. Lett.* **21** (1), 27–29.

LAUTERBORN, W. & BOLLE, H. 1975 Experimental investigations of cavitation-bubble collapse in the neighbourhood of a solid boundary. *J. Fluid Mech.* **72** (2), 391–399.

LAUTERBORN, W. & KURZ, T. 2010 Physics of bubble oscillations. *Rep. Prog. Phys.* **73** (10), 106501.

LECHNER, C., LAUTERBORN, W., KOCH, M. & METTIN, R. 2019 Fast, thin jets from bubbles expanding and collapsing in extreme vicinity to a solid boundary: a numerical study. *Phys. Rev. Fluids* **4** (2), 021601.

LECHNER, C., LAUTERBORN, W., KOCH, M. & METTIN, R. 2020 Jet formation from bubbles near a solid boundary in a compressible liquid: numerical study of distance dependence. *Phys. Rev. Fluids* **5** (9), 093604.

LI, T., ZHANG, A.-M., WANG, S.-P., CHEN, G.-Q. & LI, S. 2019 Nonlinear interaction and coalescence features of oscillating bubble pairs: experimental and numerical study. *Phys. Fluids* **31** (9), 092108.

OBRESCHKOW, D., BRUDERER, M. & FARHAT, M. 2012 Analytical approximations for the collapse of an empty spherical bubble. *Phys. Rev.* E **85** (6), 066303.

PLESSET, M.S. & CHAPMAN, R.B. 1971 Collapse of an initially spherical vapour cavity in the neighbourhood of a solid boundary. *J. Fluid Mech.* **47** (2), 283–290.

POPINET, S. & ZALESKI, S. 2002 Bubble collapse near a solid boundary: a numerical study of the influence of viscosity. *J. Fluid Mech.* **464**, 137–163.

PROUSSEVITCH, A.A. & SAHAGIAN, D.L. 1998 Dynamics and energetics of bubble growth in magmas: analytical formulation and numerical modeling. *J. Geophys. Res.: Solid Earth* **103** (B8), 18223–18251.

RATTRAY, M. 1951 Perturbation effects in cavitation bubble dynamics. PhD thesis, California Institute of Technology.

RAYLEIGH, LORD 1917 VIII. On the pressure developed in a liquid during the collapse of a spherical cavity. *Lond. Edinb. Dublin Philos. Mag. J. Sci.* **34** (200), 94–98.

REUTER, F., CAIRÓS, C. & METTIN, R. 2016 Vortex dynamics of collapsing bubbles: impact on the boundary layer measured by chronoamperometry. *Ultrason. Sonochem.* **33**, 170–181.

REUTER, F., GONZALEZ-AVILA, S.R., METTIN, R. & OHL, C.-D. 2017 Flow fields and vortex dynamics of bubbles collapsing near a solid boundary. *Phys. Rev. Fluids* **2** (6), 064202.

REUTER, F. & METTIN, R. 2018 Electrochemical wall shear rate microscopy of collapsing bubbles. *Phys. Rev. Fluids* **3** (6), 063601.

REUTER, F. & OHL, C.-D. 2021 Supersonic needle-jet generation with single cavitation bubbles. *Appl. Phys. Lett.* **118** (13), 134103.

SATO, Y. & SHIMA, A. 1980 The collapse of an initially spherical bubble near a solid wall. *Rep. Inst. High Speed Mech. Tohoku Univ.* **42**, 1–24.

SCHLICHTING, H. & GERSTEN, K. 2003 *Boundary-Layer Theory*. Springer Science & Business Media.

SHAW, S.J., SCHIFFERS, W.P. & EMMONY, D.C. 2001 Experimental observations of the stress experienced by a solid surface when a laser-created bubble oscillates in its vicinity. *J. Acoust. Soc. Am.* **110** (4), 1822–1827.

SHIMA, A. & TOMITA, Y. 1981 The behavior of a spherical bubble near a solid wall in a compressible liquid. *Ingenieur-Archiv* **51** (3), 243–255.

SOYAMA, H. 2015 Surface mechanics design by cavitation peening. *J. Engng* **2015** (13), 110–114.

VOGEL, A., BUSCH, S. & PARLITZ, U. 1996 Shock wave emission and cavitation bubble generation by picosecond and nanosecond optical breakdown in water. *J. Acoust. Soc. Am.* **100** (1), 148–165.

VOGEL, A., LAUTERBORN, W. & TIMM, R. 1989 Optical and acoustic investigations of the dynamics of laser-produced cavitation bubbles near a solid boundary. *J. Fluid Mech.* **206**, 299–338.

VOS, H.J., DOLLET, B., VERSLUIS, M. & DE JONG, N. 2011 Nonspherical shape oscillations of coated microbubbles in contact with a wall. *Ultrasound Med. Biol.* **37** (6), 935–948.

YANG, Y.X., WANG, Q.X. & KEAT, T.S. 2013 Dynamic features of a laser-induced cavitation bubble near a solid boundary. *Ultrason. Sonochem.* **20** (4), 1098–1103.

ZENG, Q., AN, H. & OHL, C.-D. 2022 Wall shear stress from jetting cavitation bubbles: influence of the stand-off distance and liquid viscosity. *J. Fluid Mech.* **932**, A14.

ZENG, Q., GONZALEZ-AVILA, S.R., DIJKINK, R., KOUKOUVINIS, P., GAVAISES, M. & OHL, C.-D. 2018*a* Wall shear stress from jetting cavitation bubbles. *J. Fluid Mech.* **846**, 341–355.

ZENG, Q., GONZALEZ-AVILA, S.R. & OHL, C.-D. 2020 Splitting and jetting of cavitation bubbles in thin gaps. *J. Fluid Mech.* **896**, A28.

ZENG, Q., GONZALEZ-AVILA, S.R., TEN VOORDE, S. & OHL, C.-D. 2018*b* Jetting of viscous droplets from cavitation-induced Rayleigh–Taylor instability. *J. Fluid Mech.* **846**, 916–943.

ZHAO, R., XU, R.-Q., SHEN, Z.-H., LU, J. & NI, X.-W. 2007 Experimental investigation of the collapse of laser-generated cavitation bubbles near a solid boundary. *Opt. Laser Technol.* **39** (5), 968–972.